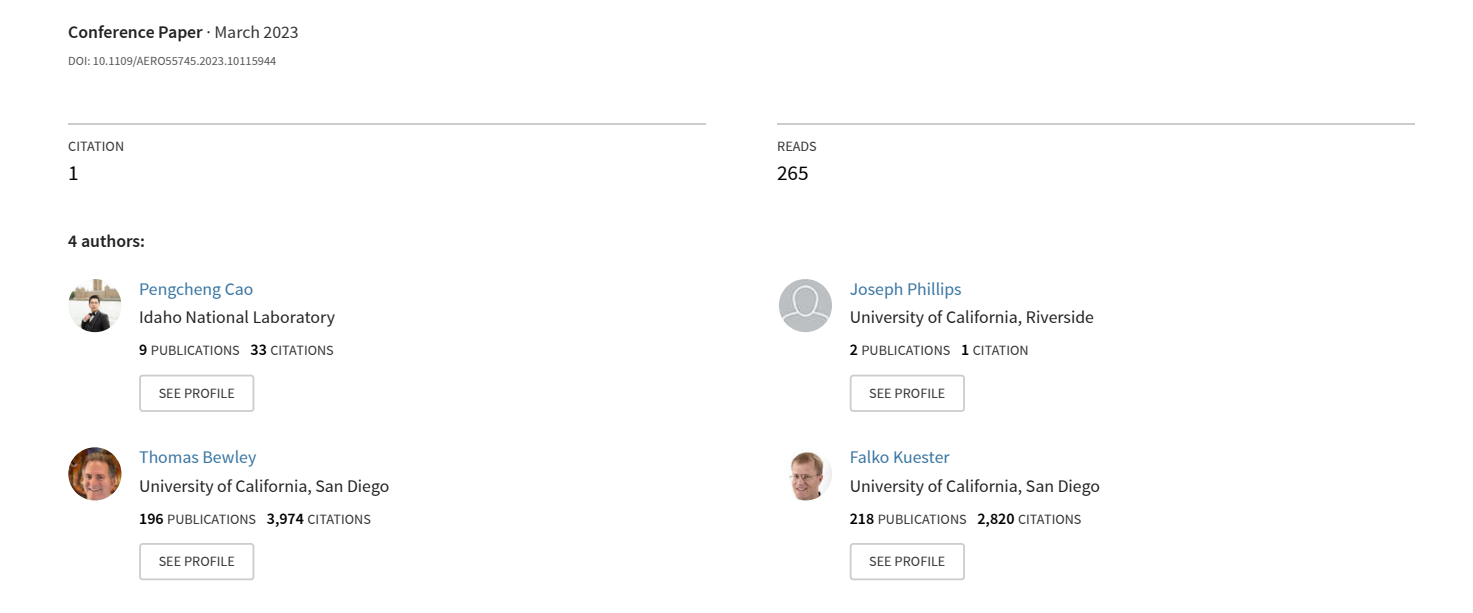
QuadGlider: Towards the Design and Control of a Bio-Inspired Multi-Modal UAV with Compliant Wings



QuadGlider: Towards the Design and Control of a Bio-Inspired Multi-Modal UAV with Compliant Wings

Pengcheng Cao Dept. of Mechanical Engineering University of California, San Diego 9500 Gilman Dr, La Jolla, CA 92093 p5cao@eng.ucsd.edu

Thomas Bewley
Dept. of Mechanical Engineering
University of California, San Diego
9500 Gilman Dr, La Jolla, CA 92093
bewley@eng.ucsd.edu

Joseph Phillips
Dept. of Mathematics
University of California, San Diego
9500 Gilman Dr, La Jolla, CA 92093
jophilli@ucsd.edu

Falko Kuester Dept. of Structural Engineering University of California, San Diego 9500 Gilman Dr, La Jolla, CA 92093 fkuester@eng.ucsd.edu

Abstract-Multirotors have become the most popular UAV or aerial robot category due to their structural simplicity and ability to take off and land vertically. However, most multirotors suffer from short airborne time and range due to limited battery capacity. Thus we propose a novel hybrid multirotor design, QuadGlider, to increase its capability of traveling long distances with minimal battery consumption. QuadGlider is inspired by the body structure and gliding mechanism of gliding animals. The airframe design of QuadGlider imitates flying squirrels' skeletal and muscular structure with implementation of servo motor to actuate its compliant membrane wings. Therefore, it can transition from quadrotor flight mode to forward gliding mode via morphing and lowering motor speeds to save power. In this work, we first present the conceptual design of QuadGlider. Next, we model its flight dynamics in different gliding scenarios. Then, the design is verified in computational fluid dynamics simulations of gliding scenarios with angles of attack of $0^{\circ} - 30^{\circ}$. At last, preliminary gliding experiments are conducted at low Revnolds numbers of around $Re = 4.7 \times 10^5$. The equilibrium glide simulation gives a maximum glide ratio of $4.\overline{27}$: 1 at a takeoff velocity of 14.0 m/s, while the experimental result indicates a glide ratio of 2.97:1 at a takeoff velocity of 4.17

TABLE OF CONTENTS

1. Introduction	
2. BACKGROUND OF BIO-INSPIRATION	
3. CONCEPTUAL DESIGN	3
4. FLIGHT DYNAMICS	4
5. AERODYNAMIC VALIDATION	8
6. EXPERIMENTAL RESULT	10
7. CONCLUSION	11
ACKNOWLEDGMENTS	11
REFERENCES	11
BIOGRAPHY	13
APPENDIX	14

1. Introduction

In recent years various micro and small unmanned aerial vehicles (UAV) are developed and deployed to perform aerial tasks where compact sizes are required (of \leq 2-meter dimensions) or close flight range (\leq 50 km) can meet such needs [1]. The micro to small-sized UAVs, depending on

the needs of realizing multiple flight modes on a single UAV have triggered the emergence of a number of multi-modal and hybrid designs. Some of the multi-modal UAVs featuring propulsion of tiltable propellers include fully-actuated multirotors [3] [4] [5] [6] [7] and tilt-rotor quad-plane UAVs [8] [9] [10]. Apart from tilt-rotors, fixed-wing vertical takeoff and landing (FW-VTOL) UAVs [11] [12] [13] [14] are developed to take off, land, and hover as a rotary-wing drone but perform fixed-wing cruise flight during most of missions. The other FW-VTOL hybrid designs include tail-sitter UAVs [15] [16] [17] which take off and land vertically on their tails and pitch forward to transition to cruise flight after taking off. The aforementioned design ideas, however, incorporated rigid wings for lift generation which generally required more mechanical power to lift off the aircraft compared to their compliant or flexible counterparts [18] [19]. Moreover, actuable compliant wing surfaces were proved to be advantageous over conventional rigid ailerons in terms of increasing roll control authority [20] [21].

the ways they produce lift, can be further categorized into

fixed-wing, rotary-wing, and flapping-wing [2]. However,

In fact, various novel UAV designs with compliant membrane wings were proposed and studied thanks to bio-inspirations. Gerdes et al. [22] developed the Robo Raven which is a birdinspired flapping-wing UAV which is able to actuate each of the two highly compliant wings independently. Abdulrahim et al. [23] presented a micro aerial vehicle design with morphing membrane wings to validate the roll control scheme of twisting the wing tips instead of using ailerons. These two designs indicate that membrane wings can be successfully applied on micro to small UAVs to generate lift but each incorporates only one single flight or locomotion mode. Shin et al. [24] [25] presented a multi-modal robot inspired by Pteromyini or flying squirrels which is able to achieve both locomotion modes of walking and gliding while can also control its angle of attack using robotic legs and tail during the flight. This design, however, cannot take off and land vertically or hover in its airborne mode. Karasek et al. [26] [27] presented the designs of several robotic hummingbirds capable of performing near-hover and forward flapping flight. Ma et al. [28] [29] presented the design and control of Havard Robobee which is a coin-sized micro aerial robot which can perform vertical take-off, hovering, and maneuvering of its flight directions. However, although flapping wings could have higher efficiency than did propellers in hover propellers [30], flapping-wing UAVs consumed significantly higher power than fixed membrane-wing UAVs during cruise or glide since flapping would increase the induced drag

978-1-6654-9032-0/23/\$31.00 ©2023 IEEE

considerably [31].

This paper presents the initial design work of a multi-modal UAV, namely QuadGlider, with four rotors and retractable membrane wings. One of the key innovations of this design is the hybrid of a bio-inpired glider UAV with compliant wings and a quadrotor which can take off and land vertically and hover in the air. In its glider mode, QuadGlider is able to perform stable high-angle-of-attack (HAoA) gliding with low aspect ratio (LAR) of wings and at low Reynolds number $(< 10^6)$. The primary contributions of this work are listed as follows: first, we review and compare the flight mechanisms of flying squirrels and flying lizards both capable of gliding flights as the main sources of bio-inspiration. Second, we propose the conceptual design of the quadrotor-glider with membrane wings and morphing mechanism. Third, we presents the modeling and simulation of its flight dynamics in two gliding scenarios. Last but not least, we validate the gliding ability of this design via computational fluid dynamics (CFD) simulations and preliminary experimental tests.

The structure of this paper is therefore: Section 2 introduces the gliding animals inspiring the proposed design; Section 3 presents the conceptual design of the wings, the fuselage, and the morphing mechanism; Section 4 derives the equations of motion and flight dynamics of QuadGlider in different flight scenarios; Section 5 presents the CFD simulations of gliding QuadGlider at various AoAs; Section 6 presents the results of a preliminary gliding test to validate the design; Section 7 delivers the conclusion and discussion of future work.

2. BACKGROUND OF BIO-INSPIRATION

In this section we will introduce the animals which provide bio-inspiration for this research project. On one hand, we will introduce *Pteromyini* tribe or flying squirrels in terms of their body structure and gliding kinematics. On the other hand, we will review *Draco* genus or flying lizards for their gliding ability and retractable wings.

Flying Squirrels

Pteromyini is a tribe of around 50 species of squirrels under the Sciuridae family which can utilize their muscles and membrane wings to perform gliding in unstructured environment like forests. Despite their misleading commonly known name as flying squirrels, Pteromyini cannot achieve full flight like bats or birds. However, their body structure can help them produce lift for them to transport from higher tree branches or leaves to lower ones by gaining lateral speed component from aerodynamics and gravity. It is learned from previous research [32] that some Pteromyini don't perform gliding in force equilibrium during most of their flight as shown in Fig. 1. The sum of lift, drag, and gravity will produce a non-zero net force for the flying squirrel to change its gliding trajectory, and such net force is modulated by fast re-deployment of membrane wing using its muscles. For QuadGlider, we will utilize servo motors to actuate morphable membrane wings in order to produce similar gliding ability as simulated in Section 4.

In addition, *Pteromyini* have evolved several body features for better maneuvering the posture for gliding. Patagia are the membrane wing structures attached to the limbs of a gliding mammal. For flying squirrels, two plagiopatagia stretch between each pair of fore limb and hind limb as shown in Fig. 2 and they are the main source of lift in the flight.

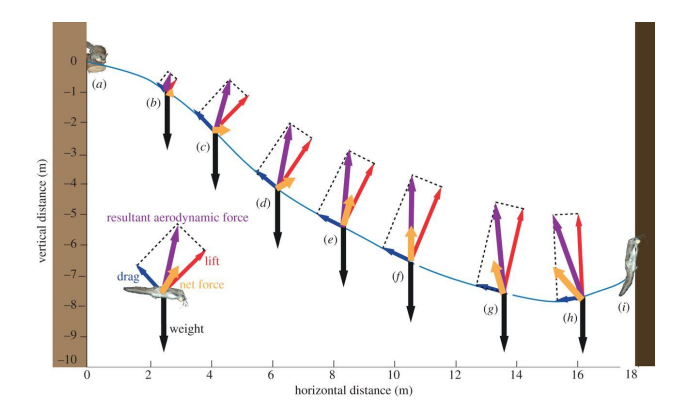


Figure 1: Simulation of a flying squirrel's non-equilibrium gliding flight to land on a tree (figure reused from [32] with permission of Royal Society Publishing).

Apart form two plagiopatagia, a flying squirrel also has two pieces of propatagia between each fore limb and its head, and two pieces of uropatagia between each hind limb and its tail. These extra membranous muscles can improve its agility as well as decrease the aspect ratio (to around 1.0) which allows flying squirrel to glide at higher angle of attack and produce more drag to decelerate for gentler landing. Moreover, the platysma, tibiocarpallis, and semitendinosus are a group of muscle structures located at the edges of the membrane wings to help hold their shapes and reduce undesired membrane fluctuations and edge fluttering during gliding. And the existence of wingtips, on the other hand, will produce wingtip vortices in gliding to reduce the induced drag exerted on the body [33].

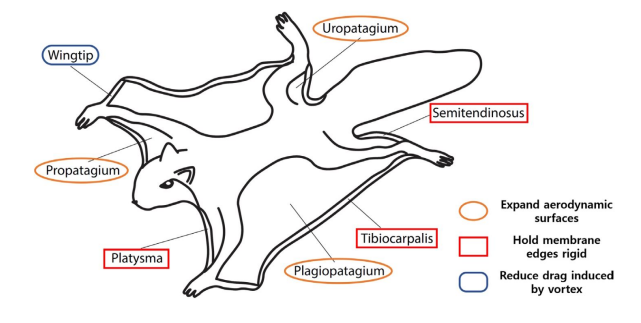


Figure 2: Body structure schematic of a flying squirrel (figure reused from [24] with permission of IEEE Explore).

Flying Lizards

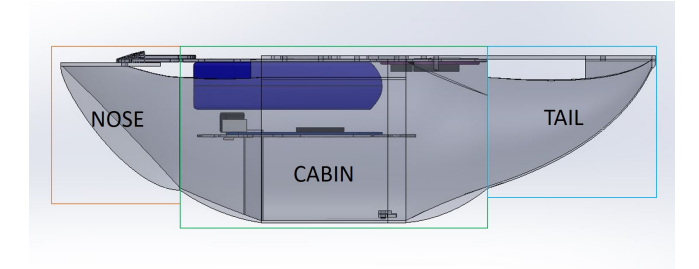
Draco or flying lizards are a genus of lizards under Agamidae family which is capable of gliding and landing on trees with retractable membrane wings. Again, flying lizards cannot achieve full flights but can utilize their patagia supported by elongated ribs to generate lift for gliding [34]. Different from flying squirrels, Draco fold their membrane wings using their muscles after landing and unfold them when they leap away to take off. In addition, some research indicates that flying lizards can achieve equilibrium or quasi-equilibrium glide [35] by observing a plateau in measured velocity profiles. A newer work, however, claims that such equilibrium glide was not observed in their gliding experiments with flying lizards [36]. And in the same paper Khandel and Hendrick proposed a novel approach for measuring the real-time body posture and airfoil orientation and camber in gliding by utilizing only 5 motion capture landmarks. In this work we adopt the ideas of reaching equilibrium glide and simplified model of aircraft configurations from aforementioned studies of flying lizards' gliding behavior.

3. CONCEPTUAL DESIGN

In this section we will introduce the design concept of multiple components of the QuadGlider prototype. The basis of QuadGlider is a quadrotor with 4 DC motors and 10-inch propellers as thrusters, and each of the rotors is positioned at one of the four corners of a $540mm \times 540mm$ square. However, in order to achieve better aerodynamic performance as a quadrotor-glider, a number of original quadrotor components need to be altered. We will first present the fuselage design and explain the design principles for it. Next, we will discuss the design of flexible membrane wings and the bioinspiration behind this idea. Last but not least, we will present the morphing mechanism serving the UAV's multi-modes and explain the four-bar linkage mechanism for wings expansion and retraction.

Fuselage Design

The fuselage design of QuadGlider is generally attributed to the following 3 principles. First, the geometry of the fuselage is designed to be spacious enough to house the avionics and Li-Po battery while being inspired by fuselages of VTOL and fixed-wing aircrafts instead of adopting the common square-shaped quadrotor fuselage. Second, the fuselage cross-sections can serve as part of overall airfoils to modulate airflow for stable gliding. Last but not least, the fuselage plays a great role in weight distribution of the aircraft such that the CoM is set to be ahead of the neutral point (NP) for pitch stability concerns [24] and beneath the wing chord lines to enhance roll stability which is inspired by the anatomy of flying squirrels [37].



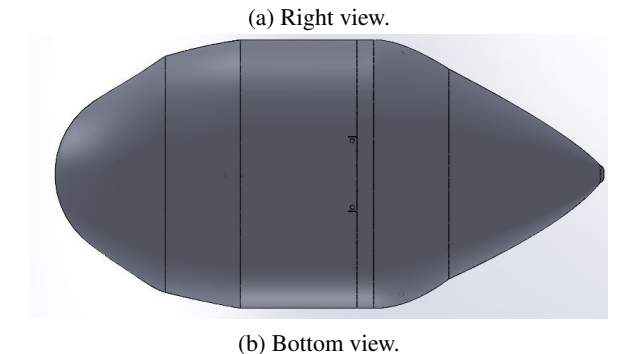


Figure 3: QuadGlider fuselage design.

The preliminary fuselage design of QuadGlider is shown in Fig. 3. The critical dimension constraints of the fuselage are the width and length of the Holybro S500 power distribution board, which are 117.9 and 196.8 mm, respectively.

Therefore, the maximum width of the cabin is set to be 160.4 mm, and maximum height 89.1 mm making this widest section of cabin half of a elliptic cylinder. And the fore-to-aft longitudinal length of the fuselage is 329.5 mm from nose's start to tail's end. The reason to have a wide cabin is on one hand to house a 14.8 V 4S Li-Po battery, a BeagleBone Blue flight controller board, and an electronical speed controller (ESC) board as shown in 3a and on the other hand to include another support board from Holybro S500 kit (119.8 \times 119.8 With its shell manufactured with glycol modified polyethylene terephthalate (PETG) via 3D-printing, the mass of fuselage is 633 g, taking 66.9% of the total mass of the vehicle (946 g). And the CoM position is measured to be 38.3 mm ahead of and 15.8 mm below the neutral point of the membrane wings which conforms to the roll stability margin [25] and makes the CoM stay inside the fuselage.

Membrane Wings Design

The wings design of QuadRotor is featuring bio-inspired compliance and inherent roll stability for gliding. On one hand, the bio-inspired compliant membrane wings, mimicking the flight behavior of flying mammals and flying lizards, can achieve a higher lift slope and stall at much higher angle of attack compared to their rigid counterparts [38]. On the other hand, some birds' flying behavior indicates that a positive dihedral angle can largely enhance the roll stability when gliding at low Reynolds number ($10^3 \sim 10^5$) [39]. As shown in Fig. 5b, the sideslip or banking will introduce a lateral airflow velocity component U_{∞} . Due to positive wing dihedral, the effective angle of attack α_{eff} of the lower wing with respect to U_{∞} will be smaller than that of the upper wing. Therefore, having the same airfoil geometry, the lower wing can produce a larger lift than do the upper wing, resulting in a roll moment in the opposite direction of the roll angle therefore hindering the increase of roll rate.

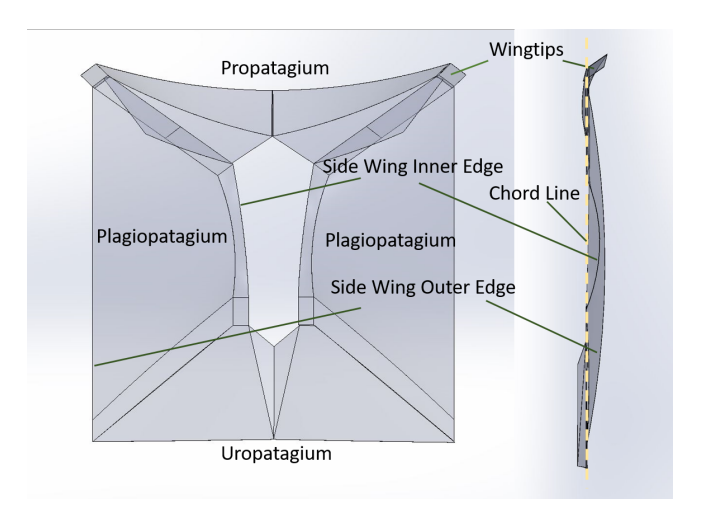
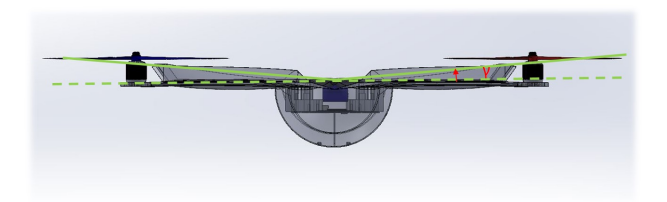
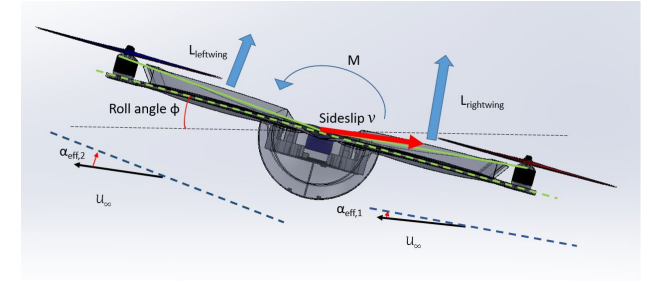


Figure 4: Membrane wing components.

The composition of the membrane wing is illustrated in Fig. 4 with both top view and left view. Analogous to the wing components of a flying squirrel, we have one Propatagium or fore membrane, two Plagiopatagia or side wings, one Uropatagium or aft membrane, and two wingtips located at the end of two front arms which is useful for reducing induced drag by generating wingtip vortices [25]. We manufactured each membrane using ripstop nylon which is a lightweight woven fabric resistant to tearing and ripping and often used for hot air baloons and wingsuits. In addition, each wing edge



(a) Positive wing dihedral.



(b) Illustration of inherent roll stability. Here the right wing will generate more lift than does the left wing in a sideslip v therefore producing a roll moment countering the increase of roll rate.

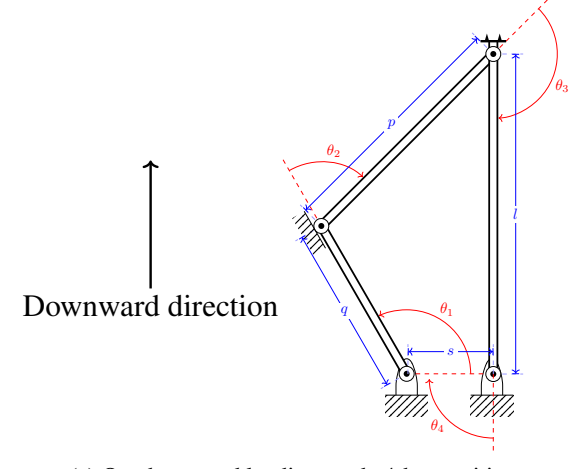
Figure 5: QuadGlider wing dihedral.

is embedded with aluminum wire to hold the wing shape and reduce membrane fluctuations. The total area of membrane wings is measured as $270,515 \ mm^2$, while the total mass is merely 103 g including the aluminum wires. As shown in the left view of Fig. 4, we can approximately find the position of the chord line and therefore simplify various membrane wing airfoils to be a non-symmetrical cambered airfoil for further analyses in pitching and gliding in XZ-plane.

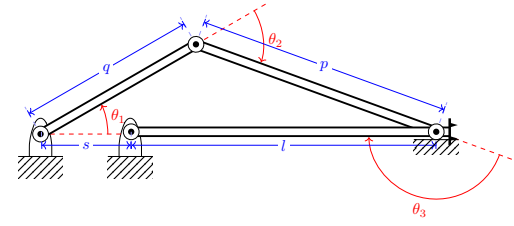
In addition, the shape of fortified membrane wings can form a positive wing dihedral angle of $\gamma=5.1\,\mathrm{deg}$. This helps the QuadGlider resist roll moment disturbance and restore the roll angle to zero during low Reynolds number gliding. However, the roll stability cannot be assured merely by the wing dihedral, and instead both the rotors and morphable wings can serve as robust source of roll moments making the QuadGlider design advantageous in maintaining roll stability.

Morphing Mechanism

Morphing between QuadGlider's quadrotor mode and glider mode is realized via four 4-bar linkages attached to each of the rotor arms. Beneath each rotor arm, a drag-link 4-bar linkage mechanism is installed to expand and retract wings to change the effective membrane wing areas under different flight modes. The illustration of the 4-bar linkage mechanism used here is shown in Fig. 6. We design the frame or fixed link to be of s=40mm and the output link or wing expansion bar to be of l=150mm. The input link or crank is set to be q = 80mm and the coupler link is p = 122mm. Therefore this mechanism satisfy s + l ensuringcontinuous circular motions for both crank and output link. A servo motor is used to drive q-bar or input link at the left fixed hinge in Fig. 6a. And the actuable part of membrane wings is attached to all four l-bars or wings expansion bars pointing towards each of the rotors. The linkage will form a quadrilateral in quadrotor mode to face the bottom of landing gear towards downward direction as shown in Fig. 6a. And it will also form a triangle in glider mode as shown in Fig. 6b. With these two scenarios as two extreme positions, QuadGlider has the ability to vary the effective lift-generating wing area continuously between these two positions to resist



(a) Quadrotor and landing mode 4-bar position.



(b) Glider mode 4-bar position.

Figure 6: 4-bar linkage configurations.

disturbance or perform maneuvers during gliding.

With aforementioned design elements and morphing mechanism introduced in this section, we can now present the assembly of QuadGlider prototype in both full-wing glider mode and quadrotor mode as in Fig. 7.

4. FLIGHT DYNAMICS

In this section, we want to investigate the flight dynamics of QuadGlider's both modes of flight, namely quadrotor mode and glider mode. The commonly-used quadrotor equations of motion (EoM) is first presented and followed by variations for transitioning into glider mode. While in terms of QuadGlider's glider mode dynamics, its gliding motions are categorized by whether the vehicle is at force equilibrium or not and also by its different configurations. As inspired by both flying lizards [35] and flying squirrels [32], QuadGlider is designed to develop a constant velocity with fixed gliding angles as well as break the force equilibrium by morphing the wing shape to land on and perch to inclined surfaces.

For the analyses in gliding flights, we make the following 2 assumptions to simplify the dynamical model: (1) we formulate all the analyses on the 2-dimensional sagittal or longitudinal plane of the UAV. By doing this we focus only on the pitch dynamics and stability which primarily affects the lift (C_L) and drag (C_D) coefficients in its flight. However, although QuadGlider's left-right symmetry ensures inherent lateral force balance, we will still discuss its lateral static stability to withstand sideslip disturbance. (2) We assume all the wing surfaces to be planar and only count their projections on the XY-plane of QuadGlider's body frame as wing surface areas. And we assume the chord lines of thin airfoils of QuadGlider's membrane wings are parallel to the XY-plane.



(a) Demo of 4-bar linkage on a rotor arm.





(b) fully expanded glider mode.

(c) Quadrotor mode.

Figure 7: QuadGlider design assembly.

Flight with Mode Transition

QuadGlider is designed to be a multi-modal UAV which can transition between quadrotor and glider flight modes. In order to smoothly perform mode transitions, we incorporate the morphing configurations as well as dynamics-based flight controls. On one hand, the morphing mechanisms has been presented and discussed in Section 3. On the other hand, the transition-related flight dynamics is investigated and discussed in this section.

We start the derivation of QuadGlider's flight dynamics with defining the coordinate systems. First, we define the Earthfixed inertial frame $\mathcal{F}_{\mathcal{E}}: \{O_E - X_E Y_E Z_E\}$. The Earth-fixed inertial frame $\mathcal{F}_{\mathcal{E}}$ denotes the inertial frame of reference fixed on the Earth and its origin and X, Y, and Z-axes align with those of the pre-flight body frame, respectively. Second, the body frame $\mathcal{F}_{\mathcal{B}}$: $\{O_B – X_B Y_B Z_B\}$ is fixed on the vehicle body and its origin coincides with the CoM. The three axes of body frame conform to the NED convention [40], with X-axis pointing out the nose of the vehicle, Y-axis pointing out right, and Z-axis pointing out the bottom. Last, the gliding frame $\mathcal{F}_{\mathcal{G}}: \{O_G - X_G Y_G Z_G\}$ also has its origin coinciding with the CoM, while its X-axis points out the direction of gliding velocity, Y-axis coincides with Y_B and Z-axis points out the opposite direction of its lift which is perpendicular to gliding velocity. The presence of gliding frame $\mathcal{F}_{\mathcal{G}}$ helps compute the lift and drag being exerted on the UAV CoM with respect to its gliding direction. The simplified right-view illustration of coordinate systems is showed in Fig. 8 with a focus of studying XZ and pitch motions.

The flight dynamics of a quadrotor UAV has been thoroughly studied in the literature [41] [42], such that we only adopt the final nonlinear form of the quadrotor EoM as

$$\dot{\mathbf{x}} = \mathbf{f}(\mathbf{x}) + \mathbf{g}_1(\mathbf{x})\mathbf{u}_1 + \mathbf{W}_{\mathbf{ext}},\tag{1}$$

where the 12-dimensional state vector and 4-by-1 quadrotor input wrench vector are

$$\mathbf{x} = [\mathbf{x} \ \mathbf{y} \ \mathbf{z} \ \psi \ \theta \ \phi \ \dot{\mathbf{x}} \ \dot{\mathbf{y}} \ \dot{\mathbf{z}} \ \mathbf{p} \ \mathbf{q} \ \mathbf{r}]^{\mathrm{T}},$$

$$\mathbf{u}_{1} = [\mathbf{F}_{\mathbf{z}} \ \tau_{\mathbf{x}} \ \tau_{\mathbf{y}} \ \tau_{\mathbf{z}}]^{\mathrm{T}},$$
(2)

respectively. x, y, z, and $\dot{x}, \dot{y}, \dot{z}$ are the displacement and velocity components in the $\mathcal{F}_{\mathcal{E}}$, respectively. And ψ, θ, ϕ are the rotational displacement components in $\mathcal{F}_{\mathcal{E}}.p, q, r$ are rotational rates with respect to x, y, z-axes of the $\mathcal{F}_{\mathcal{E}}$. And \mathbf{W}_{ext} represents the disturbance of external aerodynamic wrenches caused by wind. However, for QuadGlider in mode transition, we need also incorporate its aerodynamic wrenches exerted by its membrane wings. These forces are considered as the second control input \mathbf{u}_2 .

Accordingly, we model the aerodynamic forces exerted on the CoM of the vehicle during its glide. Similarly to the force expressions in [25], we express the force vector in \mathcal{F}_G as

$$\mathbf{u_2} = \begin{bmatrix} -D_G \\ 0 \\ -L_G \end{bmatrix} = \begin{bmatrix} -\frac{1}{2}\rho C_D V_E^2 S_w \\ 0 \\ -\frac{1}{2}\rho C_L V_E^2 S_w \end{bmatrix}, \tag{3}$$

where D_G and L_G are the magnitude of drag and lift in $\mathcal{F}_{\mathcal{G}}$, and their minus signs indicate both are pointing towards the negative X_G and Z_G directions, respectively. ρ is the density of air which we consider as $1.204~kg/m^3$ throughout this paper. V_E indicates the magnitude of gliding velocity in $\mathcal{F}_{\mathcal{E}}$ and is equivalent to $(\dot{x}^2+\dot{z}^2)^{1/2}$ as the UAV is assumed to only travel in XZ-plane. S_w is the total wing surface area and in equilibrium glide, the wings are fully expanded and their projected areas sum up to $0.1785~m^2$. C_D and C_L are drag and lift coefficients, respectively, and according to CFD simulation results in Section 5, at a fixed Reynolds number of 4.7×10^5 both coefficients vary with angle of attack α (AoA) and can be approximated with following two polynomials:

$$C_L(\alpha) = 0.7830 \cdot \alpha^3 - 3.8915 \cdot \alpha^2 + 3.9464 \cdot \alpha + 0.2660$$

$$C_D(\alpha) = 0.9854 \cdot \alpha^2 - 0.2190 \cdot \alpha + 0.1935,$$
(4)

with AoA α in radians. With α and the UAV pitch angle θ , one can compute the gliding angle θ_G by

$$\theta_G = \alpha - \theta \tag{5}$$

where θ_G is the gliding angle, i.e. the direction of gliding velocity and angle between X-axes of $\mathcal{F}_{\mathcal{E}}$ and $\mathcal{F}_{\mathcal{G}}$. During equilibrium glide, θ_G can also by computed by taking the arc-tangent of the ratio between the vertical and horizontal velocity component in the XZ-plane, i.e. $\theta_G = \operatorname{atan}(\dot{z}/\dot{x})$.

Therefore we can derive the rotation matrices between 3 different coordinate systems. $\mathbf{R_{EG}}$ and $\mathbf{R_{BG}}$ are rotation matrices from gliding frame $\mathcal{F_{G}}$ to $\mathcal{F_{E}}$ and $\mathcal{F_{B}}$, respectively, defined as

$$\mathbf{R_{EG}} = \begin{bmatrix} \cos\theta_G & 0 & \sin\theta_G \\ 0 & 1 & 0 \\ -\sin\theta_G & 0 & \cos\theta_G \end{bmatrix}, \mathbf{R_{BG}} = \begin{bmatrix} \cos\alpha & 0 & \sin\alpha \\ 0 & 1 & 0 \\ -\sin\alpha & 0 & \cos\alpha \end{bmatrix}$$
(6)

All in all, the Newton-Euler equation of motion of OuadGlider can be written as

$$\dot{x} = f(x) + g_1(x)u_1 + g_2(x)u_2 + W_{ext},$$
 (7)

and the details of EoM terms f(x), $g_1(x)$, and $g_2(x)$ are introduced in Eqn. 21.

Equilibrium Glide

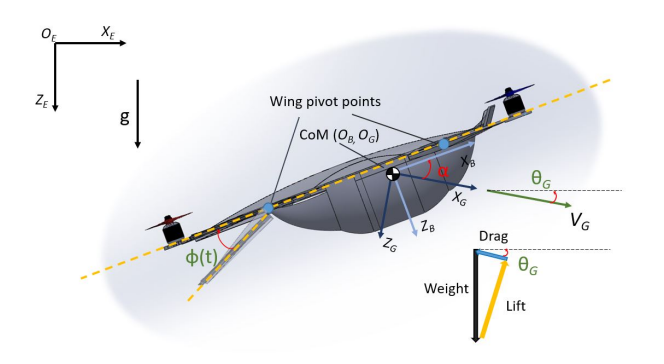


Figure 8: Definitions for QuadGlider flight dynamics and an example of equilibrium glide forces balance.

Next we can obtain the Newton-Euler equations of motion in the earth-fixed frame $\mathcal{F}_{\mathcal{E}}$ to depict the equilibrium glide dynamics. According to the definition of equilibrium glide [43], the desired glide angle can be calculated by lift-to-drag ratio at force balance:

$$\cot(\theta_G) = \frac{L_G}{D_G} = \frac{C_L(\alpha)}{C_D(\alpha)}.$$
 (8)

Therefore to describe both the translational motion in XZplane and rotational motion of body pitch, we have

$$m\ddot{\xi} = m \begin{bmatrix} 0\\0\\g \end{bmatrix} + \mathbf{R_{EG}u_2} + \mathbf{F_{ext}},$$
 (9)

$$I_{yy}\ddot{\theta} = \{\mathbf{X_{AC}} \times \mathbf{R_{BG}}\mathbf{u_2} + \tau_{\mathbf{ext}}\}_{\mathbf{y}},\tag{10}$$

where m is the mass of the UAV and I_{yy} is the y-y component of the UAV moments of inertia matrix. ξ is the UAV's position vector in $\mathcal{F}_{\mathcal{E}}$ and θ_E is the body pitch angle with respect to the Y-axis of $\mathcal{F}_{\mathcal{E}}$. Similar to the simplification of rigid body rotation of quadrotors [41] [42], the rotational acceleration of pitch angle $\ddot{\theta}$ is made equal to the time derivative of pitch rate q in body frame, and with yaw rate set to be zero, pitch moment $I_{yy}\ddot{\theta}_E$ is therefore identical to sum of torques around Y-axis. g is the gravitational acceleration (9.807 m/s^2 in this paper). \mathbf{X}_{AC} is the position

of aerodynamic center for equilibrium glide located at the quarter-chord position between the leading and trailing edges of the wings $([0.055m,0,-0.016m]^T$ in the body frame). And $\mathbf{F_{ext}}$ and $\tau_{\mathbf{ext}}$ are sum of external forces and torques caused by wind.

Non-equilibrium Glide

Non-equilibrium glide, mimicking the flight of a flying squirrel or *Draco*'s, is the gliding motion performed when there is non-zero total aerodynamic force or torque (not from wind disturbance) exerted at QuadGlider's CoM. This means either the lift, drag, and gravity will not sum up to zero or the airflow around the current configuration will generate a torque for the body angles to change over time. To track a specific gliding trajectory in non-equilibrium, *Draco*, as indicated in [36], change their body shape and posture precisely to control and modulate the aerodynamic forces. In this section, the dynamics and body posture changes are studied for QuadGlider to follow a gliding trajectory analogous to *Draco*'s gliding behavior.

The coordinate systems used for non-equilibrium glide are identical to those used in Section 4. We keep use of the inertial frame $\mathcal{F}_{\mathcal{E}}: \{O_E - X_E Y_E Z_E\}$, body frame $\mathcal{F}_{\mathcal{B}}: \{O_B - X_B Y_B Z_B\}$, and gliding frame $\mathcal{F}_{\mathcal{G}}: \{O_G - X_G Y_G Z_G\}$. However, in order to control QuadGlider's aerodynamic forces by changing its body shape, the UAV is able to change its effective wing areas attached to the rear half of the body by actuating the wing expansion bar as shown in Section 3. With the presence of a wing angle $\phi(t)$ between the front group and rear group of the wings, we model the aerodynamic forces of front and rear wing groups as

$$\mathbf{F_{G,fw}} = \begin{bmatrix} -D_{G,fw} \\ 0 \\ -L_{G,fw} \end{bmatrix} = \begin{bmatrix} \frac{1}{2}\rho C_D^{fw} V_E^2 S_{fw} \\ 0 \\ \frac{1}{2}\rho C_L^{fw} V_E^2 S_{fw} \end{bmatrix}, \tag{11}$$

$$\mathbf{F_{G,rw}} = \begin{bmatrix} -D_{G,rw} \\ 0 \\ -L_{G,rw} \end{bmatrix} = \begin{bmatrix} \frac{1}{2}\rho C_D^{rw} V_E^2 S_{rw} \\ 0 \\ \frac{1}{2}\rho C_L^{rw} V_E^2 S_{rw} \end{bmatrix}, \tag{12}$$

where fw and rw indicate the front and rear wings. We use Eqn. 4 to compute C_D^{fw} and C_L^{fw} as we now consider only the front wing groups remain fixed with the body frame. And due to the morphed wing shape, the drag and lift coefficients of rear wing groups C_D^{rw} and C_L^{rw} are therefore calculated by

$$C_L^{rw}(\alpha) = C_L(\alpha + \phi_{rw}), C_D^{rw}(\alpha) = C_D(\alpha + \phi_{rw}), \quad (13)$$

as wing angle increases the AoA of rear wing groups.

In addition, instead of having one aerodynamic center (AC) of wing groups, we now have 2 different aerodynamic centers which located at quarter-chord positions of front and rear wing groups. The front AC is at a fixed position $X_{AC,fw} = [0.110m, 0, -0.016m]^T$ in the body frame. The rear AC, however, will rotate around the CoM as wing angle $\phi_r w(t)$ changes such that

$$\mathbf{X_{AC,rw}} = \begin{bmatrix} \cos\phi_{rw} & 0 & \sin\phi_{rw} \\ 0 & 1 & 0 \\ -\sin\phi_{rw} & 0 & \cos\phi_{rw} \end{bmatrix} \begin{bmatrix} -0.140 \\ 0 \\ -0.016 \end{bmatrix}. \quad (14)$$

With aforementioned quantities, we can derive the equations

of motion for non-equilibrium glide simulation as

$$m\ddot{\xi} = m \begin{bmatrix} 0\\0\\g \end{bmatrix} + \mathbf{R}_{\mathbf{E}\mathbf{G}}(\mathbf{F}_{\mathbf{G},\mathbf{f}} + \mathbf{F}_{\mathbf{G},\mathbf{r}}) + \mathbf{F}_{\mathbf{ext}}$$
 (15)

$$I_{yy}\ddot{\theta}_E = \{ \sum_{fw}^{rw} \mathbf{X_{AC,i}} \times \mathbf{R_{BG}F_{G,i}} + \tau_{ext} \}_{y}$$
 (16)

In bio-inspired non-equilibrium glide, the QuadGlider is also designed to track a desired gliding trajectory as do *Draco* with a variable wing angle. During the non-equilibrium glide when the UAV is landing on a steep slope analogous to Draco or flying squirrels' tree perching, it needs to decrease its speed by shape changing and pitching up. Therefore a closed-loop control law is designed for it to track the desired trajectory in the landing phase and stabilize its pose as

$$\dot{\phi}(t) = -k_1(\theta(t) - \theta_{des}) - k_2\dot{\theta}(t) - k_3(x(t) - x_{des}) - k_4\dot{x}(t) - k_5(z(t) - z_{des}) - k_6\dot{z}(t).$$
(17)

Flight Simulations

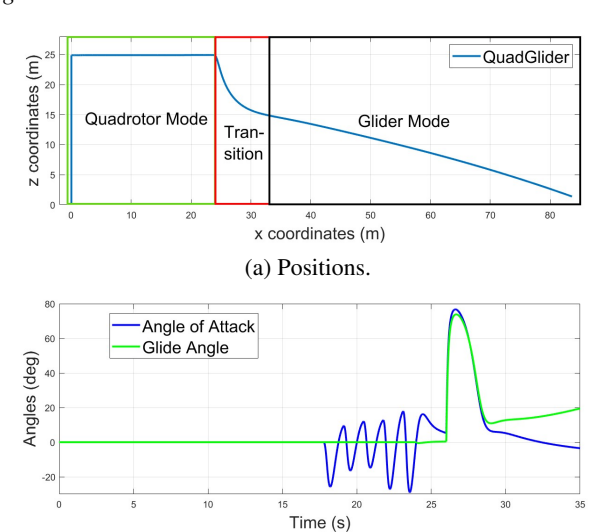


Figure 9: Flight with Transition Simulation.

(b) Angles.

In this section, we simulate the equations of motion of transition flight, equilibrium, and non-equilibrium glides numerically using MatLab. First, we set up the scenario of the flight featuring transition from quadrotor flight mode to glider. The QuadGlider takes off from the ground and stops at a height of 25 m above ground level (AGL). Then it flies forward till it arrives at $[24.0,0,25.0]^T$ m and then starts transitioning to glider mode. The transition phase takes 2.81 seconds and the QuadGlider lost altitude of 10.1 m during this period. At last the quasi-equilibrium gliding phase takes 6.29 seconds and ends at $[83.65,0,1.38]^T$ m. The simulation result of this setup is shown in Fig. 9a and 9b.

Second, we simulate the equilibrium glide by first setting up the scenario where the QuadGlider is released at a height of 30 m AGL. Both the initial angle of attack and glide angles are zero, and the initial horizontal and vertical speed components are 10 m/s and 0, respectively. The effects of external

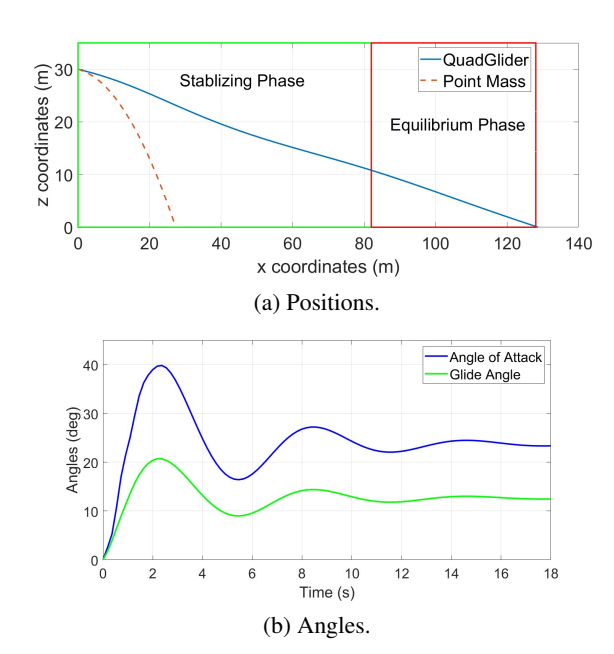


Figure 10: Equilibrium Glide Simulation.

wind are omitted in this simulation and therefore both F_{ext} and τ_{ext} are set to zero. The simulation result of this setup is shown in Fig. 10a and 10b. This glide can be divided into 2 phases, namely stabilizing phase and equilibrium phase. In the stabilizing phase ($t=0\sim 14s$, x-distance = $0\sim 82\text{m}$), the velocity vector increases from $[10,0,0]^T$ m/s to around $[12.28,0,2.61]^T$ m/s which is the equilibrium velocity. And AoA first overshoots the equilibrium AoA of 23.7° to 40° then stabilizes to the equilibrium AoA, and similarly the glide angle stabilizes to the equilibrium glide angle of 12.5° . And during the equilibrium phase ($t=14\sim 18s$, x-distance = $82\sim 128$ m), the velocity vector remains within $\pm 0.5\%$ range of $[12.28,0,2.61]^T$ and both AoA and glide angle remain close to equilibrium as well. This simulation result meets the computed equilibrium AoA and glide angle θ_G from Eqn. 8. And the overall glide ratio of this simulation is 4.27 and the equilibrium-phase glide ratio is 4.71.

Last but not least, we run the simulation of non-equilibrium glide of QuadGlider. We set the initial altitude to be 14 m AGL, and again the initial AoA and glide angle to be zero. The initial horizontal and vertical speed components are 5 m/s and 0, respectively. The simulation result of this setup is shown in Fig. 11a and 11b. This simulation can be divided into stabilizing phase, quasi-equilibrium phase, and landing phase. In the stabilizing phase ($t=0\sim 2s$, x-distance = $0 \sim 11.8 \text{m}$), the velocity vector changes from $[5, 0, 0]^T$ m/s to around $[7.73,0,2.21]^T$ m/s which is a quasi-equilibrium velocity. And AoA of both front and rear wings increase from 0 to 30° and glide angle increases to 20°. Next in the quasiequilibrium phase ($t=2\sim 5s$, x-distance = 11.8 $\sim 35m$) the AoA of both front and rear wings first increases to 38° and then decreases to 15° similarly to the angle change in the equlibrium glide simulation. And the glide angle increases to 20° and then decreases to 10° . Last, in the landing phase($t=5\sim6.5s$, x-distance = $35\sim42.4$ m), the wing shape is kept changing according to the control law depicted in Eqn. 17. The AoA of rear wings first decreases to 5° and then increases drastically to 118° at t = 6.5s, and similarly AoA of front wings decreases to 0 and then increases to 81° at

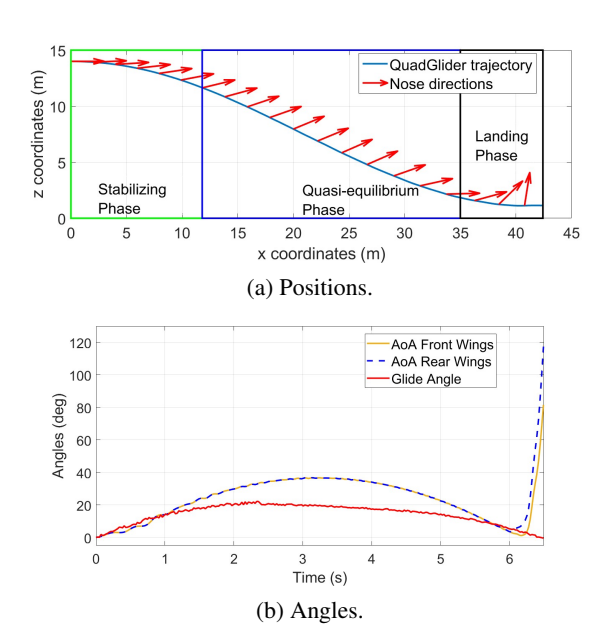


Figure 11: Non-equilibrium Glide Simulation.

t=6.5s. Therefore we can see the wing angle ϕ becomes 37° at t=6.5s. The velocity vector changes from $[8.66,0,2.01]^T$ at t=5s to $[2.18,0,0.87]^T$ at t=6.5s due to fast increased drag caused by surged AoA and pitching angle.

5. AERODYNAMIC VALIDATION

OpenFOAM Software Package

OpenFOAM is a complex open-source software consisting of multiple CFD simulation tools, including Finite Volume Method (FVM) discretization schemes [44]. The package contains both Reynolds-Averaged Naiver-Stokes (RANS) and large eddy simulation (LES) model solvers, allowing for the simulation of a wide range of Reynolds and Rayleigh numbers accompanied with either turbulent or laminar flow. These solvers have numerous different discretization methods and schemes to calculate the gradient, divergence, Laplacian, and interpolation from the discretized mesh.

All of the simulations were run using OpenFOAM with the SimpleFoam tool, which is based on Semi-Implicit Method for Pressure Linked Equations (SIMPLE) algorithm; this solves the continuity equation, momentum equation, and corrected pressure equation [45]. Since we used turbulence flow, the method we used was the $k-\omega$ model for prediction without gravity. The run time for the simulations was one second of simulation time with a write interval of .1 second. Finally, the method we choose to calculate the gradients, divergence, Laplacian, and interpolation were all Gauss linear.

Geometric Model Preparation and Mesh Generation

In Section 3, we described the development of the bioinspired QuadGlider CAD model, which was prepared for OpenFOAM using MeshMixer. The process we used in MeshMixer was to separate individual components and repair issues when exporting the SOLIDWORKS file types to mesh file types. In order to preserve high-fidelity meshing results, each of the major components was selected to be in a separate group. This methodology was performed on two meshes: a complex and simplified mesh, demonstrated by



Figure 12: The complex mesh body is on top, while the simplified mesh is on the bottom.

Fig. 12. Since the CFD simulations diverge depending on the Courant number and intersecting cells, two different meshes were used to gather additional data about the convergence and refinement levels in the mesh refinement study. When running the mesh refinement study, the computational domain's resolution was tested, requiring multiple BlockMesh variants. Other than the resolution, no further computational domain testing was done; the two computational domains that were discretized into different cell resolutions are: (36 24 6) and (18 12 1) cell amounts, producing (33.33mm 18.75mm 48mm) (66.66mm 37.5mm 288mm) resolutions from the total rectangular domain of (1200mm 450mm 288mm), respectively.

After discretizing the rectangular computational domain, we paired each face with a specific boundary-condition type; for our simulations, all the boundary conditions had type wall except for the inlet and outlet, which are given the type patch with a velocity of 15m/s and 0m/s respectively. The inlet and outlet specifications dictated the Reynolds Number, from the equation:

$$Re = \frac{uc}{v} \tag{18}$$

where v is the kinematic viscosity of air at 10° C, u is the inlet velocity, and c is the airfoil chord length. The airfoil's chord length is 447mm, yielding a Reynolds Number of 4.7×10^{5} .

Mesh Refinement Study

In order to choose an adaptive mesh refinement level converging under multiple angles of attack, we ran a mesh refinement study with various cell resolutions, cell refinement levels, and number of cells in each level. All of the mesh refinements were run with a 0 degrees angle of attack. As previously stated, the two initial discretization resolutions were (36 24 6) and (18 12 1); the refinement levels ranged from 5-8, and the number of cells in each level were either 2, 5, or 8. The entire computational domain was chosen to be in the refinement region, with an upper bound of ten million cells. After running each of the SnappyHexMesh options with both

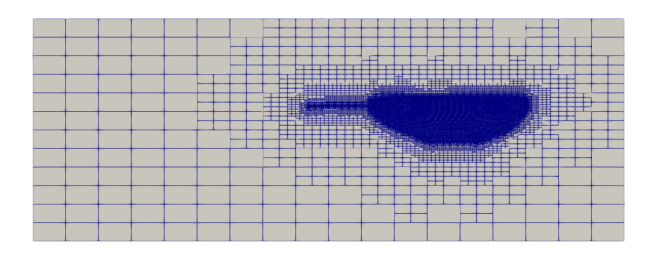


Figure 13: Mesh generated with SnappyHexMesh with a resolution of (18 12 1), a refinement level of 7, and 5 cells per level.

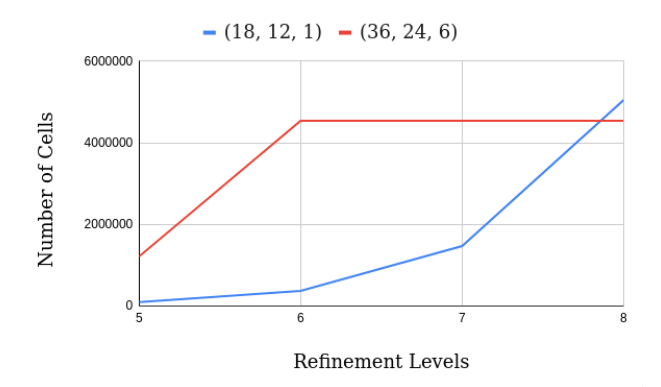


Figure 14: Graph of the refinement levels vs. number of cells with different initial resolutions.

the complex and simplified QuadGilder model, the meshes were run with SimpleFoam using the same settings described in the previous subsection, checking the pressure convergence and meshing results. See Fig. 13 for an example of the meshed computational domain.

After running all the mesh refinement variations, the CheckMesh tool was used to validate the meshes and collect the cell amounts. For the initial higher resolution computational domain, the meshing levels achieved the global maximal cell count at refinement level 6, meaning that all additional refinements after level 6 were ignored; any setting tested similarly plateaued, in both the simple or complex mesh. Fig. 14 shows a graph of the number of cells compared to the refinement levels; all other cases followed similar trajectories. Although variations between the simplified and complex mesh were minimal, there was an average of 2.8% more cells in the complex meshes compared to the simplified ones. Therefore, there was little variation loss in the overall mesh topology between using the simplified or complex initial meshes.

After running the SimpleFoam simulations on all the different mesh settings, we used Paraview to extract the drag and lift forces acting on the airfoil. In order to compare these forces' convergence between different meshes, a minimal function was run on the standard deviation of subsets of the initial data of a single force, either lift or drag, with a cardinality 8; if there were less than 8 data points, then the function was taken to be 0. The equation is:

$$\min\{\sigma(X)|X\subset I, |X|=8\}$$

where I is the initial data and σ is the method of calculating the standard deviation of a set. This was done for each

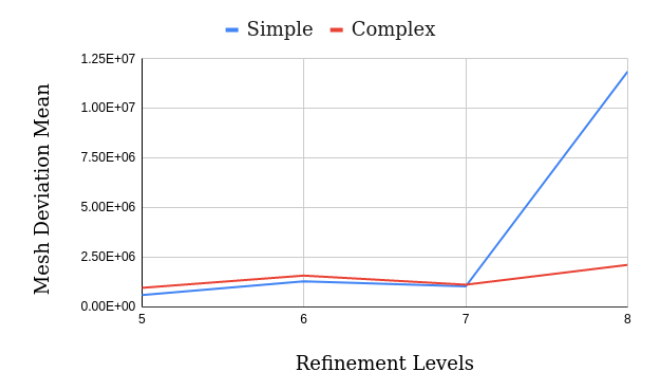


Figure 15: Graph of the refinement levels vs. the average deviation of all unique data.

setting on both the complex and simple mesh. We utilized and additional comparisons which entailed calculating the percent difference between the median force of the entire data with the medium of each simulation. In both comparison methods, the average of the two forces was then calculated and recorded. The table of the SnappyHexMesh study can be found in Table A.1.

With all the data collected and calculated, there was a large difference between the refinement levels. The consistently worse performing refinement level was 8. In the complex mesh, there were three different settings where the refinement diverged before 80% of the expected data was collected. As apparent in Fig. 15, the data converged the best in refinement levels 5 and 7. From this data, along with the previous cell count data in Fig. 14, we decided to go with a refinement level of 7 instead of 5. Even though the convergence was better with level 5 than 7, there were significantly fewer cells present in the meshing, yielding coarser results. The specific settings we went with for our angle of attack simulation were: a low resolution (18 12 1) BlockMesh, 7 refinement levels, and 5 cells per level. This produced the best complex mesh results and better than median simplified mesh results, while the median percent change was small.

Simulation Results

During the mesh analysis, a range of settings were analyzed; where a low resolution BlockMesh with 7 refinement levels and 5 cells per level produced the best results. Also, we created the simplified mesh to produce data that converged over multiple different settings, which would yield higher quality data when run with different angles of attack. The angle of attack simulation kept the same the same model (simplified), mesh discretization scheme, and SnappyHexMesh settings. We ran a simulation in SimpleFoam with angles of attack varying 5 degrees from 0 to 30. These airfoil simulations allowed us to analyze the pressure flow, coefficient of lift, and coefficient of drag at the different angles of attack.

From the airfoil simulations, we extracted streamline and contour plots to understand the behavior of QuadGlider while gliding at 15m/s wind speeds. Fig. A.1b and A.1a are the streamline plots with an angle of attack of 0. In the front and side streamline views at an angle of attack of 0, QuadGlider has relatively uniform laminar flow about the airfoil with a low pressure area on the upper surface near the wing tip. There were no present vortexes in the plot. Now compared with the plots for an angle of attack of 25 degrees in Fig. A.2b

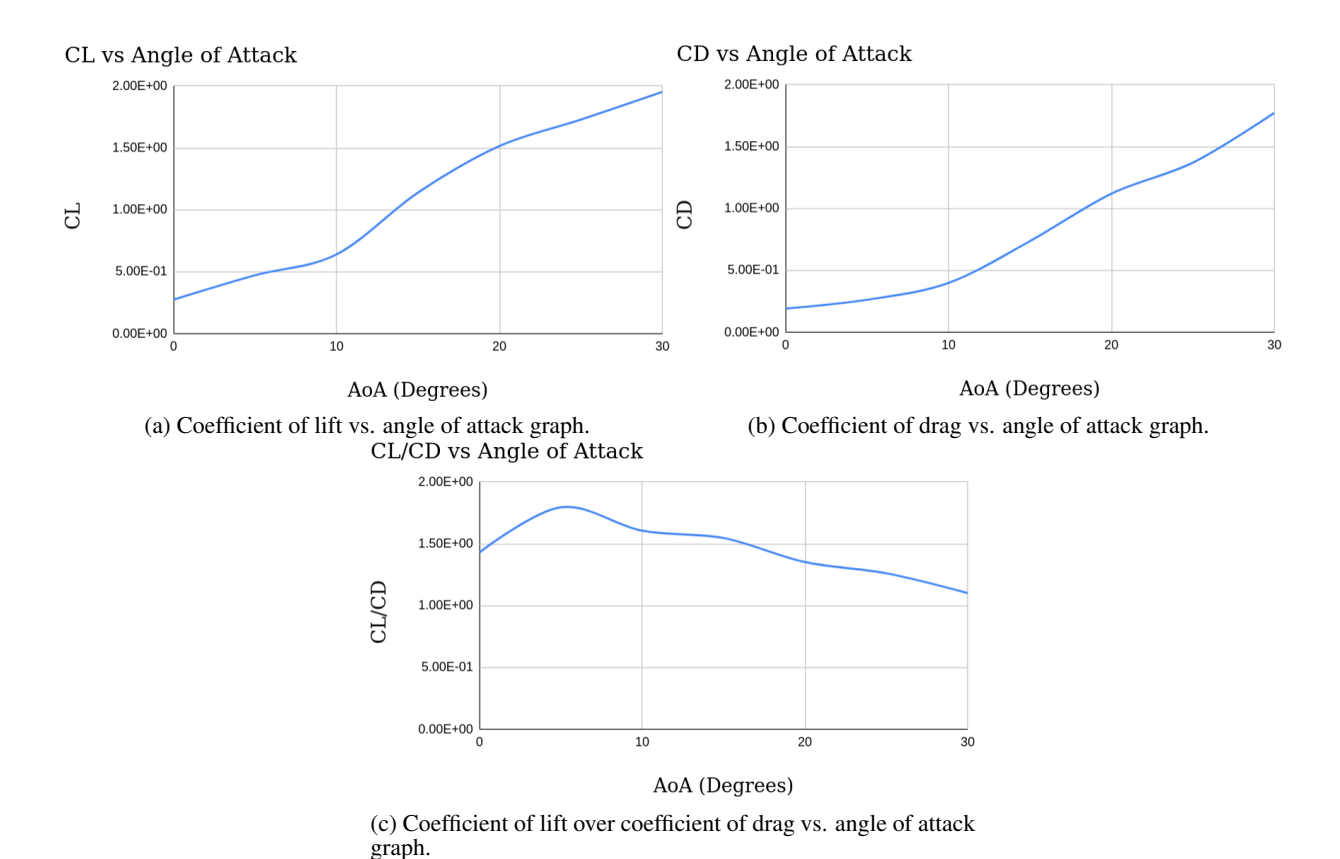


Figure 16: Variation of lift and drag coefficient for $0 - 30^{\circ}$ angle of attack.

and A.2a, the underside of QuadGlider has less uniform flow, which ends up flowing out from the side of the membrane; this is different compared with 0 angle of attack. Also, the higher angle of attack streamline has a small vortex on the membrane's upper surface. Hence the higher angles of attack will lose more speed and glide less smoothly then the lower angles of attack.

While comparing only the streamline plots is useful, it is important to also look at the contour plots, highlighting pressure flow on a specific slice of the simulation. The contour plots in Fig. A.1c and A.2c have a difference with the uniformity and distribution of the pressure flow. During the 0 degree angle of attack contour, the pressure has a small pressure deviation throughout the computational domain. On the other hand, the 25 degree angle of attack contour has larger variations on the leading edge of QuadGlider: the bottom of the membrane is high pressure, while the low is high pressure. Another difference is the regions of high and low pressure. While the 0 degree angle of attack contour has a high pressure region at the leading edge with no low pressure region, the 25 degree angle of attack contour has a high and low pressure region at the leading edge with the whole upper surface of the airfoil being low pressure. Hence, a lower angle of attack produces more uniform airflow.

After collecting the lift and drag force from the data, we calculated the coefficient of lift (C_L) and the coefficient of drag (C_D) for each angle of attack. The equations we used were:

$$C_L = \frac{2L}{\rho V_{air}^2 S_w},\tag{19}$$

$$C_D = \frac{2D}{\rho V_{air}^2 S_w}. (20)$$

With L and D as the force of lift and drag, respectively. Also, ρ is the air density of 1.204 kg/m³, V_{air} is the velocity of air 15 m/s, and S_w is the sum of the QuadGlider's effective wing

Now with the equations described above and the force data, we found the coefficient of lift and drag for each angle of attack. This data is present in Fig. 16. In Fig. 16c, any angle of attack between 0 and 30 imply that there will be a greater than 1 C_L/C_D , meaning the lift will be greater than the drag on the QuadGlider. These data points, along with measured AoA and equilibrium gliding angle in Section 6, are further fitted to polynomials and used to define the coefficients of Eqn. 4 to build a prediction model of C_L and C_D for various AoA.

6. EXPERIMENTAL RESULT

In this section we will introduce the preliminary experimental results of QuadGlider in its gliding mode. Although the primary focus of this work is the design concept and aerodynamic validation of QuadGlider, we are able to test its gliding ability by hand launching in an indoor testing setup. As expected, the QuadGlider is capable of entering equilibrium glide phase as predicted in Section 4 with fully expanded wing surface area.

Fig. 17 shows the time sequential trajectory extracted from the video footage of one of the experiments at every 0.20 s

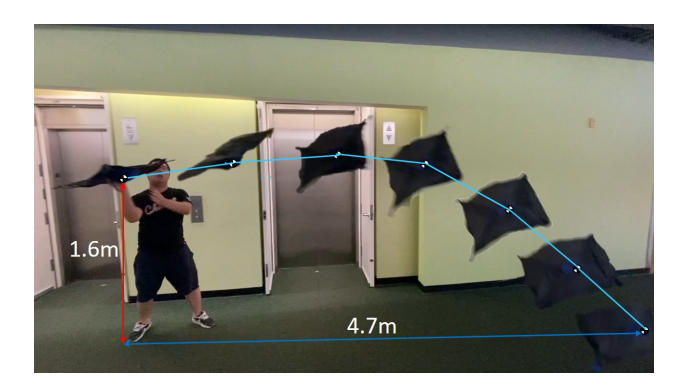


Figure 17: Time sequential trajectory of a hand-launched gliding experiment.

after the moment of launching till the UAV lands on the floor at 1.24s. The CoM position of each frame was estimated by mapping the UAV rotor positions in each frame to the ones of the original model as the rotor arms are considered rigid. We use linear interpolations here to estimate the UAV positions between 2 frames and connect these positions using light blue line segments. The launch velocity is computed as 4.17 m/s by measuring the frame positions. If we assume the QuadGlider enters equilibrium gliding phase in the last 0.6 seconds before landing, we calculate the X velocity component to be 3.68 m/s and Z velocity component 2.67 m/s at equilibrium. Therefore the gliding angle is 36.0° and the ratio of C_L/C_D is 1.3745 according to the definition of equilibrium gliding. Using Eqn. 4 we solve for the AoA $\alpha=54^\circ$ of this equilibrium phase which corresponds well with our observation in this experiment. The overall glide ratio from launching to landing is 2.97: 1 but the glide ratio in equilibrium phase is only 1.38 : 1. The other gliding experiments with QuadGlider we conducted with various but roughly controlled initial velocities also indicate this correspondence. In this case, we validate the effectiveness of our modeling for gliding.

7. CONCLUSION

We hereby reach the conclusion of this paper. First, we reviewed the body features and gliding behavior of two types of gliding animals and acquired bio-inspirations from the relevant studies. Second, design features including morphing wings, inherent roll stability, and 4-bar linkages were presented and discussed as components of conceptual design. Third, the computational fluid dynamics studies using Open-FOAM indicated the airfoil of QuadGlider would be able to modulate airflow and produce sufficient lift at $Re = 4.7 \times 10^5$ at relatively low angles of attack $(0-30^\circ)$. Last but not least, the preliminary experiment validated QuadGlider's ability of developing a equilibrium glide after being launched at 1.6m AGL, and the estimated lift and drag coefficients model corresponded well with the experimental results.

For future work, the authors would want to first investigate the potential existence of multiple equilibrium types including stable and non-stable equilibria at which Quadglider can glide to compute and achieve control authority over the desired horizontal speed in the hope of robust and reliable transition control design. In addition, the input-to-output dynamical system needs to be modeled from the servo and DC motor inputs to QuadGlider's kinematic potentially using system identification methods or analytical dynamics modeling. Last

but not least, the author would also want to achieve robust gliding control with active disturbance resistance.

ACKNOWLEDGMENTS

This publication is based on work supported by the US Army Corps of Engineers under research Cooperative Agreement W912HZ-17-2-0024 and under the auspices of the U.S. Department of Energy by Lawrence Livermore National Laboratory under Contract DE-AC52-07NA27344 and by the LLNL-LDRD Program under Project No. 20-SI-005. Additional support was provided by the Kinsella Expedition Fund. We thank all collaborators at the Qualcomm Institute, and the Contextual Robotics Institute, UC San Diego, as well as all other contributors to ideas, suggestions and comments. Opinions, findings, and conclusions from this study are those of the authors and do not necessarily reflect the opinions of the research sponsors.

REFERENCES

- [1] P. G. Fahlstrom, T. J. Gleason, and M. H. Sadraey, *Introduction to UAV systems*. John Wiley & Sons, 2022.
- [2] H. Ucgun, U. Yuzgec, and C. Bayilmis, "A review on applications of rotary-wing unmanned aerial vehicle charging stations," *International Journal of Advanced Robotic Systems*, vol. 18, no. 3, p. 17298814211015863, 2021.
- [3] D. Brescianini and R. D'Andrea, "Computationally efficient trajectory generation for fully actuated multirotor vehicles," *IEEE Transactions on Robotics*, vol. 34, no. 3, pp. 555–571, 2018.
- [4] P. Zheng, X. Tan, B. B. Kocer, E. Yang, and M. Kovac, "Tiltdrone: A fully-actuated tilting quadrotor platform," *IEEE Robotics and Automation Letters*, vol. 5, no. 4, pp. 6845–6852, 2020.
- [5] J. Strawson, P. Cao, D. Tran, T. Bewley, and F. Kuester, "Monocoque multirotor airframe design with rotor orientations optimized for direct 6-dof uav flight control," in AIAA AVIATION 2021 FORUM, 2021, p. 2431.
- [6] J. Strawson, P. Cao, T. Bewley, and F. Kuester, "Rotor orientation optimization for direct 6 degree of freedom control of multirotors," in 2021 IEEE Aerospace Conference (50100). IEEE, 2021, pp. 1–12.
- [7] P. Cao, J. Strawson, T. Bewley, and F. Kuester, "Decoupled translational and rotational flight control designs of canted-rotor hexacopters," in AIAA Scitech 2021 Forum, 2021, p. 1058.
- [8] S. Yanguo and W. Huanjin, "Design of flight control system for a small unmanned tilt rotor aircraft," *Chinese Journal of Aeronautics*, vol. 22, no. 3, pp. 250–256, 2009.
- [9] F. Kendoul, I. Fantoni, and R. Lozano, "Modeling and control of a small autonomous aircraft having two tilting rotors," *IEEE Transactions on Robotics*, vol. 22, no. 6, pp. 1297–1302, 2006.
- [10] G. R. Flores, J. Escareño, R. Lozano, and S. Salazar, "Quad-tilting rotor convertible may: Modeling and real-time hover flight control," *Journal of intelligent & robotic systems*, vol. 65, no. 1, pp. 457–471, 2012.
- [11] Ö. Dündar, M. Bilici, and T. Ünler, "Design and per-

- formance analyses of a fixed wing battery vtol uav," *Engineering Science and Technology, an International Journal*, vol. 23, no. 5, pp. 1182–1193, 2020.
- [12] S. Carlson, "A hybrid tricopter/flying-wing vtol uav," in 52nd Aerospace Sciences Meeting, 2014, p. 0016.
- [13] U. Ozdemir, Y. O. Aktas, A. Vuruskan, Y. Dereli, A. F. Tarhan, K. Demirbag, A. Erdem, G. D. Kalaycioglu, I. Ozkol, and G. Inalhan, "Design of a commercial hybrid vtol uav system," *Journal of Intelligent & Robotic Systems*, vol. 74, no. 1, pp. 371–393, 2014.
- [14] M. Tyan, N. Van Nguyen, S. Kim, and J.-W. Lee, "Comprehensive preliminary sizing/resizing method for a fixed wing–vtol electric uav," *Aerospace Science and Technology*, vol. 71, pp. 30–41, 2017.
- [15] R. Stone, "The t-wing tail-sitter unmanned air vehicle: from design concept to research flight vehicle," *Proceedings of the Institution of Mechanical Engineers, Part G: Journal of Aerospace Engineering*, vol. 218, no. 6, pp. 417–433, 2004.
- [16] D. Kubo and S. Suzuki, "Tail-sitter vertical takeoff and landing unmanned aerial vehicle: transitional flight analysis," *Journal of Aircraft*, vol. 45, no. 1, pp. 292– 297, 2008.
- [17] Y. Ke, K. Wang, and B. M. Chen, "Design and implementation of a hybrid uav with model-based flight capabilities," *IEEE/ASME Transactions on Mechatronics*, vol. 23, no. 3, pp. 1114–1125, 2018.
- [18] J. D. Eldredge, J. Toomey, and A. Medina, "On the roles of chord-wise flexibility in a flapping wing with hovering kinematics," *Journal of Fluid Mechanics*, vol. 659, pp. 94–115, 2010.
- [19] C. Kownacki and L. Ambroziak, "Local and asymmetrical potential field approach to leader tracking problem in rigid formations of fixed-wing uavs," *Aerospace Science and Technology*, vol. 68, pp. 465–474, 2017.
- [20] R. Vos, R. Barrett, R. de Breuker, and P. Tiso, "Post-buckled precompressed elements: a new class of control actuators for morphing wing uavs," *Smart materials and structures*, vol. 16, no. 3, p. 919, 2007.
- [21] M. Di Luca, S. Mintchev, G. Heitz, F. Noca, and D. Floreano, "Bioinspired morphing wings for extended flight envelope and roll control of small drones," *Interface focus*, vol. 7, no. 1, p. 20160092, 2017.
- [22] J. Gerdes, A. Holness, A. Perez-Rosado, L. Roberts, A. Greisinger, E. Barnett, J. Kempny, D. Lingam, C.-H. Yeh, H. A. Bruck *et al.*, "Robo raven: a flapping-wing air vehicle with highly compliant and independently controlled wings," *Soft Robotics*, vol. 1, no. 4, pp. 275– 288, 2014.
- [23] M. Abdulrahim, H. Garcia, and R. Lind, "Flight characteristics of shaping the membrane wing of a micro air vehicle," *Journal of Aircraft*, vol. 42, no. 1, pp. 131–137, 2005.
- [24] W. D. Shin, J. Park, and H.-W. Park, "Bio-inspired design of a gliding-walking multi-modal robot," in 2018 IEEE/RSJ International Conference on Intelligent Robots and Systems (IROS). IEEE, 2018, pp. 8158– 8164.
- [25] —, "Development and experiments of a bio-inspired robot with multi-mode in aerial and terrestrial locomotion," *Bioinspiration & biomimetics*, vol. 14, no. 5, p. 056009, 2019.

- [26] M. Karásek, "Robotic hummingbird: Design of a control mechanism for a hovering flapping wing micro air vehicle," *Universite libre de Bruxelles: Bruxelles, Belgium*, 2014.
- [27] A. Roshanbin, H. Altartouri, M. Karásek, and A. Preumont, "Colibri: A hovering flapping twin-wing robot," *International Journal of Micro Air Vehicles*, vol. 9, no. 4, pp. 270–282, 2017.
- [28] K. Y. Ma, S. M. Felton, and R. J. Wood, "Design, fabrication, and modeling of the split actuator microrobotic bee," in 2012 IEEE/RSJ International Conference on Intelligent Robots and Systems. IEEE, 2012, pp. 1133–1140.
- [29] K. Y. Ma, P. Chirarattananon, S. B. Fuller, and R. J. Wood, "Controlled flight of a biologically inspired, insect-scale robot," *Science*, vol. 340, no. 6132, pp. 603–607, 2013.
- [30] Y.-W. Chin, J. M. Kok, Y.-Q. Zhu, W.-L. Chan, J. S. Chahl, B. C. Khoo, and G.-K. Lau, "Efficient flapping wing drone arrests high-speed flight using post-stall soaring," *Science Robotics*, vol. 5, no. 44, p. eaba2386, 2020.
- [31] G. Sachs, "Comparison of power requirements: Flapping vs. fixed wing vehicles," *Aerospace*, vol. 3, no. 4, p. 31, 2016.
- [32] J. W. Bahlman, S. M. Swartz, D. K. Riskin, and K. S. Breuer, "Glide performance and aerodynamics of non-equilibrium glides in northern flying squirrels (glaucomys sabrinus)," *Journal of The Royal Society Interface*, vol. 10, no. 80, p. 20120794, 2013.
- [33] R. W. Thorington Jr, K. Darrow, and C. G. Anderson, "Wing tip anatomy and aerodynamics in flying squirrels," *Journal of Mammalogy*, vol. 79, no. 1, pp. 245–250, 1998.
- [34] A. W. Herre, "On the gliding of flying lizards, genus draco," *Copeia*, vol. 1958, no. 4, pp. 338–339, 1958. [Online]. Available: http://www.jstor.org/stable/1439979
- [35] J. A. McGuire and R. Dudley, "The cost of living large: comparative gliding performance in flying lizards (agamidae: Draco)," *The American Naturalist*, vol. 166, no. 1, pp. 93–106, 2005.
- [36] P. C. Khandelwal and T. L. Hedrick, "Combined effects of body posture and three-dimensional wing shape enable efficient gliding in flying lizards," *Scientific reports*, vol. 12, no. 1, pp. 1–11, 2022.
- [37] F. Zhao, W. Wang, J. Zhang, J. Wyrwa, and F. Sun, "Aerodynamic characteristics and pitching adjusting mechanism of the flying squirrel with deployed patagium," *IEEE Access*, vol. 7, pp. 185 554–185 564, 2019.
- [38] A. Song, X. Tian, E. Israeli, R. Galvao, K. Bishop, S. Swartz, and K. Breuer, "Aeromechanics of membrane wings with implications for animal flight," *AIAA journal*, vol. 46, no. 8, pp. 2096–2106, 2008.
- [39] A. L. Thomas and G. K. Taylor, "Animal flight dynamics i. stability in gliding flight," *Journal of theoretical biology*, vol. 212, no. 3, pp. 399–424, 2001.
- [40] G. Cai, B. M. Chen, and T. H. Lee, "Coordinate systems and transformations," in *Unmanned rotorcraft systems*. Springer, 2011, pp. 23–34.
- [41] P. Cao, J. T. Hwang, T. Bewley, and F. Kuester, "Mission-oriented trajectory optimization for search-

- and-rescue multirotor uavs in cluttered and gps-denied environments," in *AIAA AVIATION 2022 Forum*, 2022, p. 3999.
- [42] F. Sabatino, "Quadrotor control: modeling, nonlinearcontrol design, and simulation," 2015.
- [43] R. F. Stengel, *Flight dynamics*. Princeton university press, 2022.
- [44] H. Jasak, A. Jemcov, Z. Tukovic *et al.*, "Openfoam: A c++ library for complex physics simulations," in *International workshop on coupled methods in numerical dynamics*, vol. 1000. IUC Dubrovnik Croatia, 2007, pp. 1–20.
- [45] F. Moukalled, L. Mangani, and M. Darwish, "The finite volume method," in *The finite volume method in computational fluid dynamics*. Springer, 2016, pp. 103–135.
- [46] L. Daler, S. Mintchev, C. Stefanini, and D. Floreano, "A bioinspired multi-modal flying and walking robot," *Bioinspiration & biomimetics*, vol. 10, no. 1, p. 016005, 2015.

BIOGRAPHY



Pengcheng Cao received his BEng in Energy Engineering from Shandong University, China in 2016 and his MS in Mechanical Engineering from the University of California, San Diego in 2018. He worked as a project engineer in Value Wholesaler Inc. in Duarte, CA in 2018 and is currently pursuing his PhD in the Department of Mechanical Engineering at UC San Diego under the guidance of

Prof. Falko Kuester and Prof. Thomas Bewley. His research interests lie in controls and dynamic systems, robotics, and photogrammetry.



Joseph Phillips is a fourth year undergraduate Mathematics student at UC San Diego. In 2018, he worked in the USD Biophysics lab with Dr. Rae Anderson on programming DNA bead tracking code in MatLab. Currently, he is pursuing his Bachelor of Science degree in Mathematics and also working on research projects studying additive manufacturing optimization and aerody-

namics under the guidance of Prof. Falko Kuester.



Thomas Bewley (BS/MS Caltech 1989, PhD Stanford 1998) directs the UCSD Flow Control and Coordinated Robotics Labs, working at the intersection of semi-autonomous agile robotics and the analysis, estimation, and forecasting of environmental flows using advanced control theory and numerical methods.



Falko Kuester received an MS degree in Mechanical Engineering in 1994 and MS degree in Computer Science and Engineering in 1995 from the University of Michigan, Ann Arbor. In 2001 he received his PhD from the University of California, Davis and currently is the Calit2 Professor for Visualization and Virtual Reality at the University of California, San Diego. Dr. Kuester holds

appointments as Full Professor in the Departments of Structural Engineering and Computer Science and Engineer- ing and serves as the director of the Calit2 Center of Interdisciplinary Science for Art, Architecture and Archaeology, CISA3.

APPENDIX

$$\dot{\mathbf{x}} = \mathbf{f}(\mathbf{x}) + \mathbf{g_1}(\mathbf{x})\mathbf{u_1} + \mathbf{g_2}(\mathbf{x})\mathbf{u_2} + \mathbf{W_{ext}},$$

$$\text{where } \mathbf{f}(\mathbf{x}) = \begin{bmatrix} \dot{x} \\ \dot{y} \\ \dot{z} \\ q \frac{s(\phi)}{c(\theta)} + r \frac{c(\phi)}{c(\theta)} \\ p + q \cdot s(\phi)t(\theta) + r \cdot c(\phi)t(\theta) \\ 0 \\ 0 \\ -g \\ \frac{I_y - I_z}{I_x} qr \\ \frac{I_z - I_y}{I_z} pq \\ \frac{I_z - I_y}{I_z} pq \end{bmatrix}, \mathbf{g_1}(\mathbf{x}) = \begin{bmatrix} 0^{6 \times 1} & 0^{6 \times 1} & 0^{6 \times 1} & 0^{6 \times 1} \\ g_1 & 0 & 0 & 0 & 0 \\ g_2 & 0 & 0 & 0 & 0 \\ g_3 & 0 & 0 & 0 & 0 \\ 0 & 1/I_{xx} & 0 & 0 & 0 \\ 0 & 0 & 1/I_{yy} & 0 & 0 \\ 0 & 0 & 0 & 1/I_{zz} \end{bmatrix}, \text{ and } (21)$$

$$\mathbf{g_2}(\mathbf{x}) = \begin{bmatrix} 0^{6\times1} & 0^{6\times1} & 0^{6\times1} \\ c(\theta_G) & 0 & s(\theta_G) \\ 0 & 1 & 0 \\ -s(\theta_G) & 0 & c(\theta_G) \\ 0 & 0 & 0 \\ z_{AC} \cdot c(\alpha) + x_{AC} \cdot s(\alpha) & 0 & z_{AC} \cdot s(\alpha) - x_{AC} \cdot c(\alpha) \\ 0 & 0 & 0 \end{bmatrix}, \text{ additionally }$$

$$g_1 = -\frac{1}{m} [s(\phi)s(\psi) + c(\phi)c(\psi)s(\theta)]$$

$$g_2 = \frac{1}{m} [c(\psi)s(\phi) - c(\phi)s(\psi)s(\theta)]$$

$$g_3 = -\frac{1}{m} [c(\phi)c(\theta)].$$

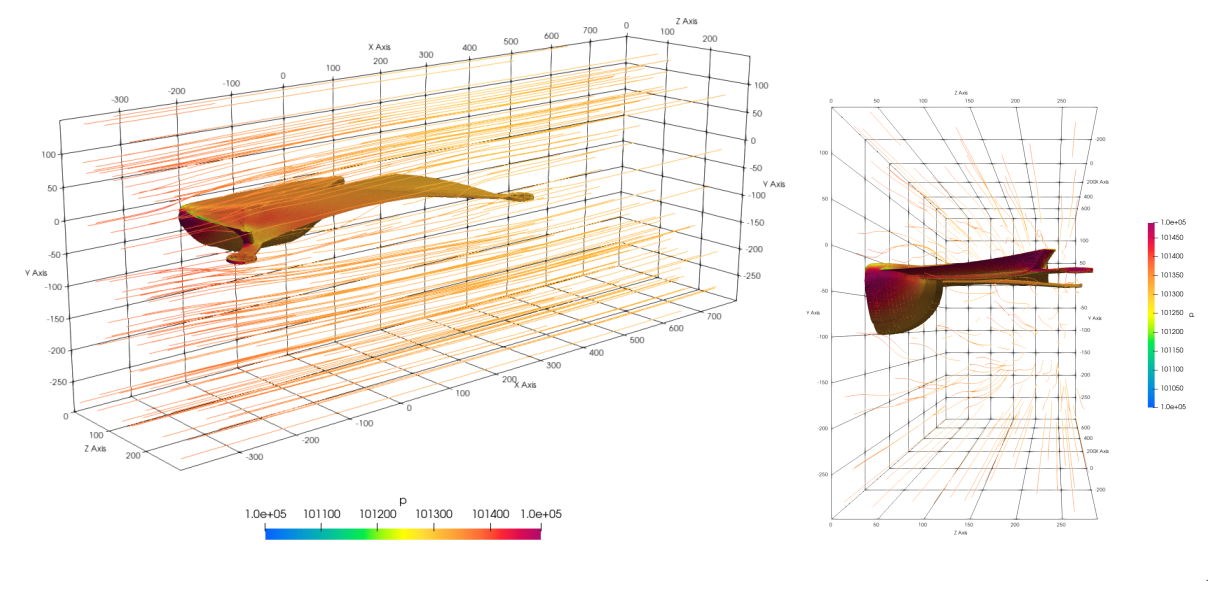
In Eqn. 21, $c(\cdot)$ and $s(\cdot)$ represent $\cos(\cdot)$ and $\sin(\cdot)$ functions, respectively. I_{xx} , I_{yy} , and I_{zz} are the diagonal terms of QuadGlider's moments of inertia matrix. In our case, they are 2.621×10^{-2} , 5.326×10^{-2} , and 3.021×10^{-2} $kg \cdot m^2$, respectively. θ_G and α are the gliding angle and AoA, respectively. With the equilibrium assumption, they are computed by

$$\theta_G = \arctan(\frac{\dot{z}}{\dot{x}}), \ \alpha = \theta_G + \theta.$$

Last but not least, x_{AC} and z_{AC} are the X and Z component of the position of aerodynamic center in $\mathcal{F}_{\mathcal{B}}$. For QuadGlider, the aerodynamic center \mathbf{X}_{AC} is measured to be $[0.055, 0, -0.016]^T$ m.

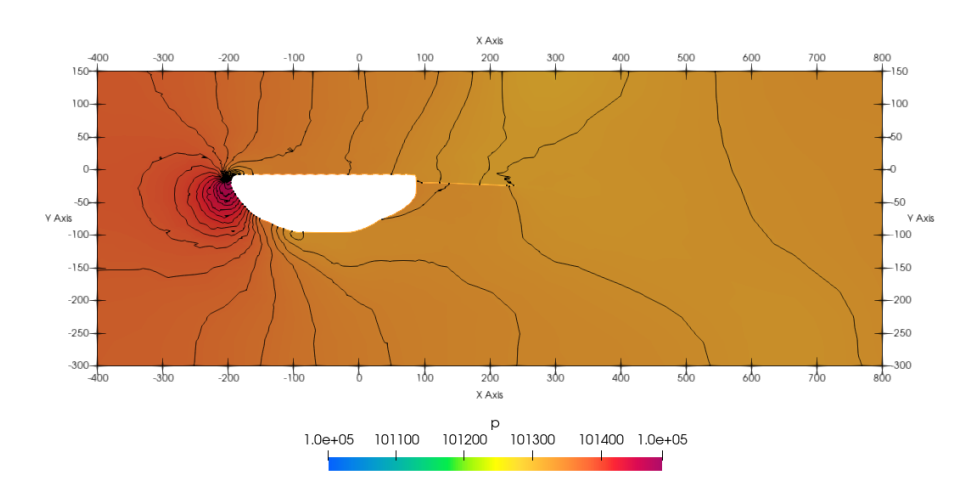
Blocks	Refinement Levels	Cells Per Level	Simplified Mesh σ	Complex Mesh σ	Median %-Change
(18 12 1)	8	8	7.39E+05	2.12E+06	0.91
(18 12 1)	7	8	2.11E+06	1.24E+06	0.77
(18 12 1)	6	8	2.02E+06	8.00E+05	6.28
(18 12 1)	5	8	1.00E+06	7.65E+05	6.74
(18 12 1)	8	5	7.32E+05	0	2.76
(18 12 1)	7	5	7.33E+05	2.09E+05	6.03
(18 12 1)	6	5	9.31E+05	2.19E+06	4.66
(18 12 1)	5	5	4.77E+05	2.68E+05	10.71
(18 12 1)	8	2	3.41E+07	0	0.45
(18 12 1)	7	2	2.67E+05	1.92E+06	667.82
(18 12 1)	6	2	8.38E+05	2.83E+06	3.09
(18 12 1)	5	2	2.21E+05	5.35E+05	10.89
(36 24 6)	6	8	2.37E+06	0	1.26
(36 24 6)	5	8	1.12E+06	3.15E+06	0.45
(36 24 6)	6	5	1.02E+06	1.12E+06	1.25
(36 24 6)	5	5	3.99E+05	6.46E+05	0.57
(36 24 6)	6	2	5.45E+05	9.55E+05	1.25
(36 24 6)	5	2	3.28E+05	4.08E+05	0.47

Table A.1: Refinement and convergence studies for all unique simulations.



(a) Pressure streamline plot side view.

(b) Pressure streamline plot front view.



(c) Contour plot of a slice at 30mm.

Figure A.1: Pressure plots at an AoA of 0 degrees.

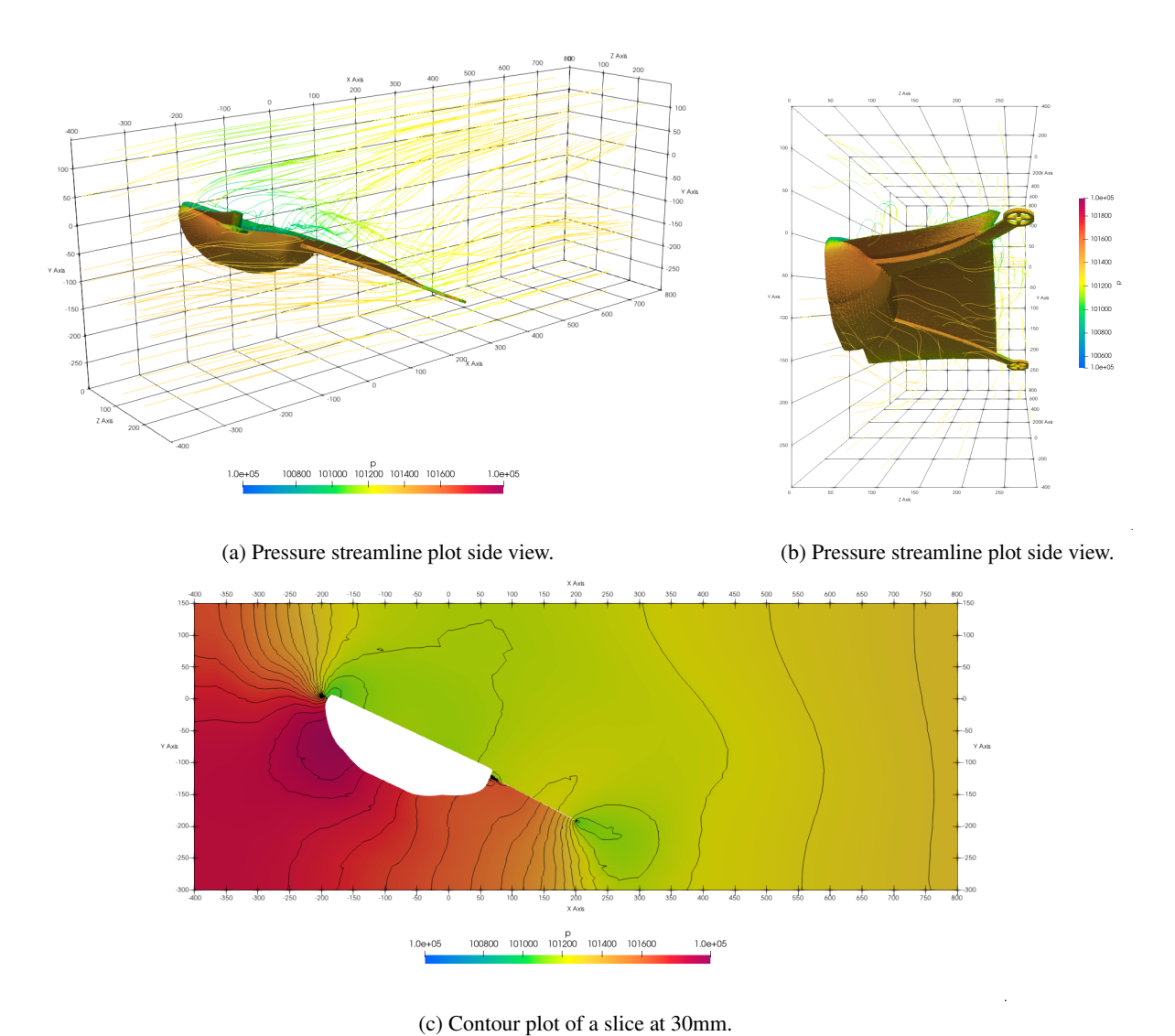


Figure A.2: Pressure plots at an AoA of 25 degrees.